PCCP

Accepted Manuscript

ROYAL SOCIETY OF CHEMISTRY

www.rsc.org/pccp

Characterizing the nanoclay induced constrained amorphous region in model segmented polyurethane-urea/clay nanocomposites and its implications on gas barrier properties

Sangram K. Rath,[1]Kathi Sudarshan,[2] Rupesh S. Bhavsar,[3]Ulhas K. Kharul,[3] Pradeep K. Pujari,[2] Manoranjan Patri,[1*] Devang V. Khakhar [4]

[1]Polymer Division, Naval Materials Research Laboratory, Shil-Badlapur Road, Ambernath-421506, Maharashtra, India
[2]Radiochemistry Division, Bhabha Atomic Research Centre, Mumbai-400085, Maharashtra, India
[3]Polymer Science & Engineering Division, National Chemical Laboratory, Pune-411008, Maharashtra, India
[4]Department of Chemical Engineering, Indian Institute of Technology, Bombay Powai, 400076, Mumbai, India

Abstract

There has been an increasing recognition of the fact that purely geometric factors associated with clay platelet dispersion in a polymer matrix cannot adequately explain the barrier properties of polymer/clay nanocomposites. The objective of the present work is to understand the nanoclay induced structural changes in a polyurethane-urea matrix and clay dispersion at different length scales using segment specific characterization techniques and implications of the same in gas barrier properties using He, N_2 and CO_2 as probe molecules. Wide angle x-ray diffraction (WAXD) and positron annihilation life time spectroscopy (PALS) studies revealed nanoclay induced alterations in the chain packing of the amorphous soft segments of the polyurethane matrix at a molecular scale of a few armstrongs. The hard segment organization and phase morphology of the nanocomposites, spanning length scales of several nanometers, were investigated by small angle x-ray scattering (SAXS), scanning electron microscopy (SEM) and atomic force microscopy (AFM). Further, the presence of constrained amorphous region surrounding the nanoclay was confirmed from AFM, WAXD and PALS results. Several pertinent structural variables from the gas transport point of view were deduced from these characterization techniques to understand the effect of the barrier properties in tandem with the clay dispersion morphology.

Key words: Nanoclay, constrained region, polyurethane, barrier property

*Corresponding author: email: mrpatri@gmail.com; Phone:+91-2512623137

Introduction

Incorporation of a small fraction of nanoclay in a polymer matrix has shown significant improvement in gas and liquid barrier properties subject to realization of nanoscale dispersion of the clay platelets.[1-4] The decrease in penetrant permeability in such hybrid systems is a function of the aspect ratio of the clay platelets, their volume fraction and orientation. Both experimental[4-7] and theoretical studies[8-10] reveal that the improvement in barrier properties of polymer/clay nanocomposites (PCN) is due to impermeable clay layers effecting tortuous pathway for a permeant traversing the nanocomposite. The tortuosity effect in turn is directly related to the dispersion state of the clay nanoplatelets. It has also been shown that purely geometric factors cannot adequately explain the barrier properties of PCNs.[11-13] The nanoclay induced changes in the structure of the polymer matrix is also an important factor in deciding the ultimate barrier properties of PCNs besides the geometric parameters. Experimental results in several PCNs[14-24] show that incorporation of nanofillers including nanoclay, leads to reduction in segmental mobility of chains in the vicinity of the surface of the nanofillers. This in turn leads to the creation of an immobilized polymer layer with properties significantly different from the unaffected bulk. This region has been nomenclatured as the interphase, constrained region or bound polymer layer by various research groups. [14-24] As regards its implications on gas barrier properties, the polymer in this region can be expected to have a lower free volume owing to the reduced segmental mobility and therefore a lower diffusion coefficient than the bulk. Adame and Beall[12] showed the existence of nanoclay induced constrained region governs the barrier properties of PCNs, using Nylon-6 as the host matrix. They directly visualized and quantified the constrained region from atomic force microscopy (a staggering 98% at 5 wt% clay loading) and posited that a correction factor (taking into account the diffusion coefficient of the constrained region) applied to the geometric model would accurately predict the barrier properties of PCNs. Xu *et al.*[13]developed a permeability model including chain-segment immobility as a factor besides the geometric parameters associated with nanoclay orientation, to understand the chain confinement from clay layers in PCNs. The results showed that the chain confinement enhanced the barrier properties of the intercalated nanocomposites. However, the universal applicability of the model is limited by the lack

of experimental data on evaluation of chain-segmental mobility factor, especially for amorphous polymers. Similarly the effect of interphase characteristics, interaction of the constituents of PCN with penetrant molecules,[11] free volume changes [25-28] and the clay induced constrained chain dynamics[12,13,29] on the barrier properties of PCNs have been reported for various polymeric systems.

Segmented polyurethanes have been popular host matrices in the field of PCNs to study the barrier properties.[30-34] However, most of the studies have been limited to polyether based polyurethanes. The objective of the present work is to understand the mechanistic origin of the barrier properties of nanoclay filled segmented polybutadiene polyurethane-urea matrix. This system can be considered as a model one for investigation of transport and morphology relationships in segmented block copolymers [35-37] because of (a) absence of hydrogen bonding between the soft and hard segments (b) higher degree of micro-phase separation and the amorphous nature of the soft segments and (c) possibility of direct visualization of hard domain morphology by microscopic techniques. There are several reports on the morphology-gas transport correlations of these model systems.[38-41] However, to the best of our knowledge, this is the first report on the transport behavior of PCNs derived from polybutadiene polyurethanes. In a recent paper we reported the mechanistic origin of the multi-scale mechanical properties of this system.[42] We demonstrated that the polymer chains in the proximity of nanoclay are constrained because of their interactions with the well-dispersed nanofillers, and these constrained polymer chains contributed to the enhancement of the mechanical properties from *nano* to *macro* scale.

The objective of the present work is to understand the nanoclay induced structural changes in the polymer matrix in terms of the constrained soft segment dynamics, diminished interchain spacing and free volume as structural parameters besides the geometrical parameters associated with nanoclay dispersion that might influence the barrier properties of the PCNs. Furthermore, a comprehensive analysis of the clay dispersion in the polyurethane matrix is carried out using complimentary techniques of x-ray diffraction, scattering as well as direct visualization by TEM, SEM and AFM.

Experimental

Materials

Hydroxyl terminated polybutadiene (HTPB) ($M_n \approx 2694$ g/mole, functionality 2.4,) was provided by Orion India Pvt. Ltd. Isophorone diisocyanate (IPDI) from Fluka, 4,4′-methylene bis(o-chloroaniline) (MOCA) from Setco Chemicals (Mumbai, India), sulfur free toluene from S. D. Fine Chem. (Mumbai, India) and dibutyltin dilaurate (DBTDL) from Aldrich were used as received. The nanoclay additive used in this study is commercial modified montmorillonite clay, referenced as Cloisite 10A, with a specific gravity of 1.9 g/cm^3, supplied by Southern Clay Products (Gonzales, TX, USA). Cloisite 10A is dimethyl benzyl hydrogenated-tallow ammonium montmorillonite clay. The organic content in the organoclay is 39.6% with a d_{001} spacing of 19.2 Å as per specifications provided by the manufacturer.

Preparation of polyurethane-urea and its nanocomposites

The details of the preparation of the nanocomposites are reported elsewhere.[42] Briefly, the aromatic diamine chain extended polyurethane-urea and its nanocomposites were prepared by a two step process consisting of synthesis of prepolymer using hydroxyl terminated polybutadiene (HTPB) and isophorone diisocyanate (IPDI), followed by chain extension with 4,4′-methylene bis(o-chloroaniline) (MOCA) using toluene as the solvent. The prepolymer was synthesized by reacting dried HTPB and IPDI (molar ratio of IPDI:HTPB:: 2:1) with DBTDL catalysis (0.05 wt%) in dried toluene in a three necked 500 ml flask under dry nitrogen atmosphere. The reaction was carried out at 70°C under mechanical stirring for 6 h. In the second step the excess isocyanate of the prepolymer was reacted with stoichiometric quantity of the MOCA (NCO: NH_2 (molar ratio): 1:1) at 70°C until the total consumption of the free NCO. The nanocomposites were prepared by premixing 1, 3 and 5 wt% of nanoclay in HTPB and then in-situ preparation of the nanocomposites following the same procedure as adopted for the neat polyurethane-urea synthesis. The hard segment content was kept constant (21%) by using a predetermined amount of polyol, diisocyanate, and chain extender. The neat polyurethane-urea and the nanocomposites with 1, 3 and 5 wt% clay content are referred to as PBDPU, PBDPU-1, PBDPU-3 and PBDPU-5, respectively.

Membrane preparation

For gas transport studies ~200 μm films were prepared, by solution casting method. The nanocomposite dispersions in toluene (~50 vol. % solid content) were cast in a Teflon mould by an applicator to wet film thicknesses of ~400 μm, so as to yield dry free standing films of the required thicknesses. The films were dried in a vacuum oven at 80°C for 6 hours to obtain dry free standing films.

Characterization

Wide angle x-ray diffraction

WAXD studies were carried out for the samples by using Cu-K_α ray of wavelength 1.54 Å at a scan rate of 0.2°/10 sec using a Philips X-ray diffractometer.

Small angle x-ray scattering

Small angle x-ray (SAXS) measurements were carried out using a Rigaku small angle goniometer mounted on rotating anode x-ray generator (CuKα). Scattered x-ray intensity $I(q)$ was recorded using a scintillation counter with pulse height analyzer by varying the scattering angle 2θ where q is the scattering vector given by $4\pi.\sin(\theta)/\lambda$ and λ is the wavelength of incident x-rays. The intensities were corrected for sample absorption and smearing effects of collimating slits.

Scanning electron microscopy

The morphology of the air-, substrate interfaces and fracture surface of the nanocomposites was investigated by using field emission scanning electron microscopy (Carl Zeiss Supra 55VP Field Emission SEM), equipped with an Oxford instrument energy dispersive x-ray spectroscopy (EDS) system. Samples were prepared by cryogenic fracture by dipping samples into liquid nitrogen for 10 min and then fracturing (bending mode) with two pliers and the imaging was carried out at an accelerating voltage of 20 kV. All the samples were gold-coated by means of a sputtering apparatus under vacuum before observation.

Atomic force microscopy

Morphological analyses of polyurethane and nanocomposite surfaces were carried out using a Digital Instruments make NanoScope IV multimode atomic force microscope. Imaging was performed in tapping mode using a microfabricated silicon cantilever (40 N/m, Veeco, Santa Barbara, CA) in air.

Positron annihilation lifetime spectroscopy

Positron annihilation lifetime measurements of the nanocomposite samples were carried out at room temperature using a fast-fast coincidence spectrometer. The time resolution of the positron lifetime spectrometer measured for gamma-rays of ^{60}Co was 270 ps. A 20 μCi ^{22}Na positron source was sandwiched between two pieces of the same samples. The total area under each lifetime spectra was about 10^6 counts. The lifetime spectra were analyzed for discrete lifetimes using the PATFIT program [43]. All the measured spectra fitted well with three components. The first lifetime component τ_1 (~ 125 ps) and the second lifetime component τ_2 (= 300-310 ps) are attributed to the self annihilation and of parapositronium (*p*-Ps) and the free positron annihilation respectively. The third lifetime component τ_3 (τ_3 = 2-2.4 ns) results from the pick-off annihilation of o-Ps in the free volume holes. The relation between *o*-Ps lifetime and radius of the free volume is given as[44]

$$\tau_3 = \frac{1}{2}\left[1 - \frac{R}{R+\Delta R} + \frac{1}{2\pi}\sin\left(\frac{2\pi R}{R+\Delta R}\right)\right]^{-1} \qquad (1)$$

where R is the radius of the free volume hole; ΔR = 1.66Å is the thickness of the homogeneous electron layer in which the positron in *o*-Ps annihilates [45].

Gas Permeability measurements

Pure gas permeability (He, N_2 and CO_2) of PBDPU and its nanocomposites was determined using membranes with active area of 12 cm^2 and thickness of ~200 μm by variable volume method[46] at 35 °C and upstream pressure of 10 atm while maintaining the permeate side at atmospheric pressure. The purity of the gases used for the permeation studies (for He, N_2 and CO_2) was 99.9%. The gas permeability was calculated using following equation.

$$P = \frac{N \cdot l}{(p_1 - p_2)} \qquad (2)$$

where P, the permeability coefficient expressed in Barrer (1 Barrer = 10^{-10} cm^3 (STP).cm/cm^2.s.cm Hg), p_1 and p_2 are the feed and permeate side pressure (cm Hg), l is the membrane thickness (cm) and N is the steady-state penetrant flux (cm^3/cm^2/sec). Each

permeability coefficient data obtained is an average of five different measurements with a standard error of ± 3%.

Modeling of transport mechanisms

The relative permeability of the gas molecules (He, N_2 and CO_2), which corresponds to the ratio between the permeability of the nanocomposites, P_c and permeability of neat matrix, P_m was modeled by the geometrical path model proposed by Bharadwaj[8] given by:

$$\frac{P_c}{P_m} = \frac{1-\phi_i}{1+\frac{\alpha}{2}\phi_i\left(\frac{2}{3}\right)\left(O+\frac{1}{2}\right)} \quad (3)$$

In Eq. 3, the parameters involved are the volume fraction of filler, ϕ_i , the particle aspect ratio, α, and the orientation parameter of the clay platelets, O. For O= 1, Eq. 3 leads to Nielson's formula, corresponding to clay platelets perpendicularly oriented to the diffusion flux[47] and $O = 0$ corresponds to random orientation of clay platelets. The volume fraction of nanoclay in the polymer matrix has been estimated using pure component densities as follows:

$$\phi_{nc} = \frac{W_{nc}}{W_{nc} + \frac{\rho_{nc}}{\rho_{pu}}(1-w_{nc})} \quad (4)$$

where, ρ_{nc} and ρ_p are the pure nanoclay and polymer densities, respectively and w_{nc} is the nanoclay weight fraction.

Results and discussion

Nanoclay dispersion and phase morphology

The formation of nanocomposite between the polymer and nanoclay was observed by XRD, SAXS and SEM imaging. Figure 1A sows the WAXD profiles of Closite-10A and the nanocomposites in the 2θ range 3-10°. A peak at 2θ = 5.2° for curve corresponding to Cloisite 10A clay indicates an interlayer spacing d_{001} of 1.7 nm. For the PBDPU nanocomposites WAXD results show a featureless profile devoid of peaks for values of 2θ from 3 to 10°. Based on this, it is reasonable to presume that the clay layers have expanded to more than 2.8 nms, as the lowest angle probed was 3°.

SAXS was used to obtain simultaneous information on clay dispersion as well as phase morphology of the samples. Figure 1B shows the SAXS profiles ($I(q)q^2$ vs. q) of PBDPU and its nanocomposites, where $I(q)$ is the intensity of the scattered x-rays and q is the scattering vector. PBDPU-1 shows a broad but mild peak located around q = 1.5 nm^{-1}, attributed to the basal spacing of the intercalated clay platelets. The *d*-spacing of the intercalated clay platelets determined by applying the Bragg's equation was found to be 4.1 nm as against a value of 1.7 nm for Cloisote-10A nanoclay (from WAXD). Only a marginal shift of the peaks to lower scattering vectors is seen with further clay loading. This is consistent with the observations of Jang *et al*. that, if a low solubility parameter polymer (<19 $J^{1/2}/cm^{3/2}$)/modified-clay composites are prepared via in-situ polymerization, intercalated and/or partially delaminated structures are observed more readily, and the clay layers exhibit an increased *d* spacing (an intercalated structure).[48] Thus the observed intercalated morphology from SAXS can be rationalized to the lower solubility parameter of the polybutadiene SS (8.67 $cal^{1/2}cm^{3/2}$ = 17.68 $J^{1/2}cm^{3/2}$) [39] and its similarity of value with the surfactant of Cloiste-10A nanoclay (16.2 $J^{1/2}cm^{3/2}$).[48]

The presence of a phase separated structure is also confirmed from the SAXS profiles. As can be seen from the profiles, a scattering peak is observed for the neat sample as well its nanocomposites at lower q values of 0.52-0.56 nm^{-1}. The peak position is related to the interdomain distance of hard segment domains, L

$$L = \frac{2\pi}{q_{max}} \qquad (5)$$

where q_{max} is the scattering vector at which maxima in intensity is observed. This spacing represents a three-dimensional average over the sample volume. The variation of the L values with clay loading (Table-1) indicates that the interdomain spacing decreases with clay loading. From the image analysis of the TEM micrographs at different magnifications we reported,[42] an empirical aspect ratio of 18 ± 3 for the intercalated nanoclay layers using the Fornes and Paul method.[49]

Figure 2 shows the FESEM micrographs of the air-, substrate interfaces and the cross-section (freeze fractured) of the PBDPU and its nanocomposites. An initial observation that can be made from the air-, substrate and cross sectional images is that the neat polymer and the nanocomposites are dense, with no evidence of pores or

channels. First focusing on the images of the neat PDDPU matrix, roundish lumpy or raised regions with finer textures of 30-40 nm scale are discernible which are more pronounced for the air-interface than the bottom surface. We interpret these features as evidences of dispersed hard sphere morphology with spherical hard domains dispersed in a continuous soft segment matrix, in agreement with the morphological observations from TEM of this polyurethane matrix.[42] The fracture surface of the neat matrix, on the other hand, shows patch patterns believed to form during brittle, unstable fracture in glassy polymers [50] and also in elastomers. Similar fractured patterns have been reported by Zheng *et al.* for other polyurethane matrices.[51,52] The air and substrate side surfaces of the nanocomposites are characterized by the presence of bright spots on the back scattered images corresponding to distribution of organoclay particles in the bulk of the polymer matrix. A very large amount of submicron sized smaller particles appears together with a few larger ones in the 1 to 5 μm range in these composites. The degree of dispersion of the nanoclay in the PBDPU matrix was further characterized using SEM-EDS mapping. The EDS technique enables measurement of the elemental composition from the X-rays emitted during electron bombardment of a particular sample area in SEM. The spatial variation of elements in the sample can be obtained by rastering the electron beam over an area of interest known as an X-ray map.[53] A typical cross sectional mapping for PBDPU-5 is shown in Figure 3. The EDS spectra showed emission from Al and Si which derive solely from the layered aluminosilicates of the nanocomposite samples. The Si/Al ratio was found to be 2.1, close to the value (2.3) of the bulk nanoplatelet Closite-10A. Figures 3 (C) and (D) show the elemental mapping for Al and Si corresponding to the spatial arrangement of silicate layers. From the images, it can be inferred that silicate layers are randomly distributed within the polymer matrix with evidences of a few clusters of Al and Si elements consistent with the larger particulate aggregates of the size of a few microns. This indicates that the x-ray diffractogram and SAXS do not represent the entire microstructure of the nanocomposite and that a broad mixture of structures ranging from single layers to intercalated tactoids comprising of different number of layers are present. The absence of peaks in the WAXD plot could be due to the random dispersion of the primary particles with different distances among clay and their heterogeneous microstructure.[54]

The images of the fractured surfaces of the nanocomposites are in stark contrast to the neat PBDPU matrix, characterized by very rough surfaces with homogeneous distribution of the clay aggregates in the polymer surface. The images also reveal that some particles of organoclay are pulled out of the polyurethane matrix, suggesting strong interaction between the organoclay and polyurethane matrix. The significant differences in the fractured surface images of the neat PBDPU and its nanocomposites also suggest a different fracture mechanism operative in the nanocomposites. The smooth fractured surface of the neat PBDPU can be accounted for by the fact that the amorphous soft segment is able to rearrange and cover the surface of neat polyurethane. However in the nanocomposites, the soft phase cannot efficiently cover the surface as it is constrained by the interfacial interactions between the polymer and the nanoparticles. This interpretation is in accordance with the detailed interpretations of fracture behaviour of polyurethane nanocomposites by Zhang *et al.*[51,52]

Evidences of nanoclay induced constrained amorphous region

The polymer-organoclay interaction is the key to nanocomposite properties as stronger interaction leads to better dispersion and larger amount of constrained region. In polyurethane/clay nanocomposites, preferential interactions of nanoclay with segment blocks are observed depending on the polarity of the latter.[55] On the basis of closeness of solubility parameter of the polybutadiene soft segment and the clay surfactant, non polar interactions of van der Waals type is expected. As regards the hard segment and nanoclay interactions, from FTIR analysis we have shown increased degree of urethane hydrogen bonding for the nanocomposites compared to the pristine polymer.[42] We presume that these segment specific interactions, account for the existence of a sizeable volume fraction of constrained region in the nanocomposites as quantified from dynamic mechanical analysis.[42] In this section we provide further evidences of the existence of the constrained region by using WAXD, PALS and AFM.

As shown in Figure 4A, the neat polymer and the nanocomposites exhibit prominent amorphous halos in the WAXD profiles in the 2θ range 10-30°. The position of the diffraction peak can be used to ascertain the spacing between polymer chains or segments of various amorphous polymers and the packing of polymer segments in nanocomposites. From the angle of the diffraction maxima corresponding to the

amorphous halo, the intersegmental distance (*d*-spacing) can be calculated according to the Bragg's equation: $\lambda = 2dsin\theta$, where λ is the *X*-ray radiation wavelength, and *d* the intersegmental distance. Relative to the neat PBDPU, the halos shift progressively towards higher diffraction angles, implying decreasing intersegmental distance of the soft segment of PBDPU with clay loading. The results emphasize subtle molecular scale modification of polybutadiene chain packing in the polymer matrix induced by nanoclay, as these length scales are related to the basic building block of chemical bonds in polybutadiene.

PALS is a sensitive technique that can be used to probe the inter- and intra- chain space of the nanocomposites which provides a quantitative characterization of the chain packing and dynamics in terms of the size and concentration of free volume elements.[27, 56-59] The various free volume parameters i.e. free volume hole size and the fractional free volume of the samples are calculated from positron annihilation parameters and presented in Table 2. The results show that the neat PBDPU has an *o*-Ps life time and its intensity value of 2.5 ns and 16.5%, respectively which compares reasonably with the values for a polybutadiene polyurethane with equivalent hard segment contents.[38] The *o*-Ps lifetime and the radius of the free volume holes, *R* varies only marginally with clay loading with the extent of variations within the approximate 0.03 ns sensitivity of PALS technique. However, the o-Ps intensity (I_3) which is characteristic of number of free volume holes decreases appreciably with clay loading. It implies that incorporation of nanoclay affects the number density of the holes more than their size. This is consistent with observations of decreasing I_3 and invariant free volume radius, *R* upon clay loading for semicrystalline poly(m-xylene adipamide)/clay[25] and styrene-butadiene-rubber (SBR)/clay nanocomposites.[26] The decreasing I_3 and fractional free volume can be attributed to the immobilization of the soft segments around the nanoclay platelets as the constrained region can diminish the formation of free volume holes, as can be seen from the decreasing I_3 with increased constrained region fraction in Figure 5.

Figure 6 shows the topographic images of the neat PBDPU and PBDPU-1 at different magnifications. For segmented polyurethanes with rigid hard domains and flexible soft domains, contrast between the two phases results from the variation in the local stiffness of the two domains.[60-63] The high-modulus hard domains appear as light

areas, and the low-modulus soft segments appear as dark areas. From the image of the neat PBDPU, evidence of nanoscale phase separation in the polyurethane matrix is discernible from the near-surface hard blocks: yellow near spherical domains with sizes varying from 10-30 nms dispersed in a brown background (soft segment). This corroborates the observation of phase separation from SAXS analysis. From the images of PBDPU-1 at different magnifications, bright light pink spots are also seen, besides the yellow domains, which are assigned to the near surface nanoclay intercalated domains. [16,31] The images reveal fine intercalated clay stacks as well as agglomerated features, consistent with SEM imaging results. Between two given clay particles or intercalated blocks, the soft segment region has a lighter brown shade in the immediate vicinity of the particles and away from it tends to be darker in the middle region (easily delineated from the magnified image in Figure 6E). These lighter brown shades surrounding the clay blocks are ascribed to the constrained region fraction induced by nanoclay.[16] The above interpretation is again based on the fact that the AFM imaging provides a map of stiffness variation on the sample surface such that a stiffer region has a more positive phase shift and hence appears brighter.[63] This allows for a method of distinguishing surface features of different modulus. The order of stiffness for the various components of the nanocomposites can be stated as: Nanoclay (~270 GPa) [64] > Hard segment (~5 GPa) [65] > constrained soft segment > bulk soft segment (~ 5 MPa).[42] The constrained fraction region has been shown to be stiffer than the unaffected bulk in PCNs because of the lower mobility of polymer chains in this region.[17]

From the AFM images, the average spacing between the intercalated clay blocks was found to be 150-180 nms and the spatial extent of the constrained region is estimated to be 40-60 nm away from the clay surface. This is consistent with the theoretically expected range of the constrained polymer region predicted by Beall [66] to be 50–100 nm from the surface of the clay. Sikdar *et al*. reported the average thickness of the interphase to be 25 nm for a polyamide/clay nanocomposite.[16] The higher spatial extent of the constrained region in the present case could be due to the amorphous nature of the polybutadiene soft segments in contrast to the crystalline polyamide matrix. It is thus evident that the nanoconfinement effect of clay on polymer chains is not restricted only to the interlayer gallery spacing (on the order of 2-3 nm between silicate sheets), but

extends to polymers confined between silicate tactoids with length scales on the order of 100s of nm.

Gas transport properties

The transport properties of the nanocomposites, were investigated by using three probe molecules (He, N_2 and CO_2), differing in their kinetic diameters and polymer interaction capacity. The permeability coefficients of various gas molecules for neat PBDPU and its nanocomposites are shown in Table 3. From the data, it is observed that PBDPU and its nanocomposites are highly permeable to CO_2 and He but relatively less permeable to N_2: permeability coefficients are in the order of $P_{CO2} > P_{He} > P_{N2}$. The kinetic diameters of the gas molecules are in the order He (2.3 Å) < CO_2 (3.3 Å) < N_2 (3.64Å).[67] The higher permeability of He compared to N_2 (both being non-interacting type) is expected based on the kinetic diameter of these gas molecules. The higher permeability of CO_2 compared to He, despite its bigger size, is due to higher solubility of CO_2 in polyurethanes.[68] As regards the effect of nanoclay, the permeability coefficients of the gas molecules decrease with clay loading, irrespective of their size and nature in accordance with the tortuosity concept. It is established that the transport of small molecules in high soft segment content polybutadiene polyurethanes (> 60%) is dominated by the amorphous polybutadiene component.[36] This is because the transition from a dispersed hard segment domain morphology to continuous glassy phase occurs between 50 to 70% hard segment for polybutadiene polyurethane systems.[36] From the AFM images, dispersed hard segment domain morphology is clearly established in the present case. It is thus logical to expect that the nanoclay induced restricted mobility of the soft segments and consequent changes in its free volume would have a pronounced effect on the transport properties of the polyurethane matrix with a hard segment content of 21%. Utilizing the pure gas permeability coefficients, the permselectivity (α_{ij}) of the gas pairs (CO_2 / N_2 and He/N_2) was calculated using the ratio P_i/P_j and the values are given in Table 3. The polyurethane-urea membrane shows α_{ij} value of 15.5 for CO_2/N_2 (removal of CO_2 from air) and 3.2 for He/N_2 (separation of He from air).

From the free volume data presented in Table 2, it can be readily observed that the mean pore radii for all the samples (3.27-3.3 Å) are much larger than that of the gas molecules used in the present study (radius of He, N_2, CO_2 are 1.3, 1.82 and 1.65 Å,

respectively). Therefore, any small changes in pore radius would have negligible effect on gas permeability. However, from PALS results, the hole number intensity is found to decrease appreciably with clay loading for the nanocomposites. This suggests that any effect on gas transport properties will be due to the reduction in the number of pores. The gas permeability across a polymer film (*P*) and fractional free volume (FFV) of the polymer are related as: [69]

$$P = A.\exp(-B/FFV) \qquad (6)$$

The constants *A* and *B* for a particular gas depend on its molecular size and its steric and energetic interactions with the polymer backbone. Figure 7 shows the logarithm of the permeability (*P*) as a function of the reciprocal of fractional free volume for all the probe molecules. A linear relationship is observed in each case, which implies that microscopic free volume plays a dominant role in determining macroscopic barrier properties of the nanocomposites.

Model fitting

In order to better understand the barrier properties the relative permeability of various molecules, is plotted against the nanoclay volume fraction in Figure 8. The experimental data were fitted by the geometrical model based on tortuosity effects (Eq. 3) proposed by Nielsen and Bharadwaj by using root-sum-square method. The aspect ratio evaluated from the best fitting of experimental data for all the molecules with *O* = 1 and *O* = 0 are shown in Table 4. In the case of oriented particles (*O* = 1), Nielson's formula leads to α = 18-20 and for random particle orientation (*O* = 0), the best fitting experimental data was obtained with α = 50, 56 and 70 for He and N_2 and CO_2, respectively. From the TEM images a disordered or random distribution of clay platelets was seen in our earlier study on these sytems,[42] so realistically, the mean orientation parameter *O* should be taken between 0 (random) and 1 (oriented). Further, it is well-known that accurate evaluation of aspect ratio from TEM micrographs is rather difficult, due to the curvature, orientation, and flexibility of clay platelets. However, the large disparity in aspect ratios from TEM (found to be 18 ± 2) and model fitting suggests that there is an additional contribution to the barrier properties which stems from the nanoclay induced alterations in the soft segment conformation and hard segment organization which is discussed in the next subsection.

Effect of constrained region on barrier properties

In the geometrical modeling the effect of nanoclay/polymer interface is usually neglected as highlighted in several different cases.[11-13] The significant alteration in the properties of the permeable amorphous phase domain of the polyurethane matrix due to the presence of nanoclay is expected to affect the transport properties of the polymer matrix. The overall gas transport process in a polymer is a function of the polymer properties such as inter-segmental spacing, polymer segmental mobility and hence the free volume in the polymer matrix. This is especially the case for a polymer matrix in a thermodynamic state of above its glass transition temperature i.e. rubbery polymers. Owing to the restriction of polymer motion due the interaction of the polymer with the surface of the nanoclay, the constrained region can be presumed to have free volume fraction and hence gas diffusion coefficient that are significantly different than the bulk polymer.

Assuming a simple additive rule, the fractional free volume of the constrained region can be calculated as:

$$FFV_{NC} = FFV_m(1-C) + FFV_C C \qquad (7)$$

where *FFV* is the fractional free volume and the subscripts *NC*, *C* and *m* are for the nanocomposites, constrained amorphous region fraction and bulk polymer matrix, respectively. *C* is the volume fraction of polymer chains constrained in the polymer matrix.

The Eq. can be rearranged as

$$\frac{FFV_{NC}}{FFV_m} = C\left(\frac{FFV_C}{FFVm} - 1\right) + 1 \qquad (8)$$

It is noteworthy that the hard segment content has a significant effect on the free volume fraction of polyurethanes. However, for a relatively lower hard segment content polyurethane-urea, the free volume characteristics would be dominated by the soft segment. This assumption in tandem with the fact that o-Ps probe is sensitive to the molecular structure and molecular interaction present in the amorphous phase, reasonably justifies the evaluation of the free volume fraction of the constrained region through Eq. 7 by neglecting the hard segment contribution to free volume. Figure 9 shows the variation

in the normalized fractional free volume as a function of constrained region fraction. As expected, a reasonably linearly decreasing trend of relative FFV with increasing *C* is discernible from the plot. The fractional free volume for the constrained region thus calculated from the linear fitting was found to be 1.82% as against a value of 4.36% for the neat PBDPU (a staggering 56% lesser than the bulk soft segment). This points to the fact that the constrained region will be significantly less permeable to the molecules compared to the bulk unaffected region. The fundamental origin of the lowered diffusion rates in this constrained region could be the reason for an overall decreased permeability in the nanocomposites.

Another important structural variable corresponding to the interchain spacing in the amorphous phase is the *d*-spacing deduced from WAXD. We posit that this parameter can be used as the chain segment immobility factor in the model developed by Xu *et al.* [13] as given in Eq. 9.

$$R_p = \frac{(1-\phi_s)/\zeta_1}{1+\frac{L}{2}\left(\frac{w}{\phi_s}\right)^{1/2}(w+H)^{-3/2}} \qquad (9)$$

This model takes into consideration both the geometric parameters associated with nanoclay dispersion (Φ, the volume fraction of clay, length,*L* and width, *w* of the clay particles) as well the nanoclay induced chain segment immobility factor, to predict the transport properties of nanocomposites. The chain segment immobility factor is given as:

$$\zeta_1 = \exp\left[k(D-\phi_L^{1/2}/2)\right]^2 \qquad (10)$$

where *K* is a constant for different penetrants diffusing through the same film, *D* is the diameter of a penetrants, and $(\Phi_L)^{1/2}/2$ is approximately equal to mean unoccupied distance between two chain segments.[13] The interchain distance <*R*> obtained from the amorphous halos of WAXD profiles can be treated as the equivalent parameter. From Figure 4B, it is seen that <*R*> decreases exponentially with increasing clay loading or conversely with increased volume fraction of amorphous constrained region. Using the values of <*R*> from Figure 4B for $(\Phi_L)^{1/2}/2$ in Eq. 10, the ζ_1 values obtained varied from 1.77-2.23 (for N_2 as the permeating gas) with increasing clay loading.

Another concomitant effect of clay addition is the change in hard segment organization of the PBPU matrix as reported earlier from the hard sphere model fitting of SANS traces and complemented by TEM.[42] When observed in TEM, the neat PBDPU showed sparsely distributed bigger spherical hard domains. Inclusion of clay showed an increase in hard sphere volume fraction from 0.17 for neat PBDPU to 0.25 for PBDPU-5, with a decrease in the size of the hard spheres. This would mean an additional contribution towards tortuosity as the hard domains too are impermeable to the diffusing molecules as the ratio of the diffusivities of soft and hard segments of polybutadiene polyurethanes is reported to be 45 and 28 for CO_2 and N_2, respectively.[36] This contribution can be captured from the simple Maxwell model, used to predict the permeability of membranes filled with impermeable spherical nanoparticles.[70]

$$P_{eff} = P_c\left(\frac{1-\phi}{1+0.5\phi}\right) \qquad (11)$$

where P_c is the permeability of the composite medium, P_p is the permeability of the pure polymer and P_{eff} is the volume fraction of filler. According to this model a ~8% decrease in permeability for PBDPU-5 is predicted compared to the unfilled matrix, solely on the basis of the change in domain morphology. The overall transport properties in a segmented polyurethane/clay nanocomposite are thus a complex interplay of various structural variables which cannot be predicted by simple tortuosity models. While the effect of each structural parameter on the gas transport properties is discussed here in isolation, the combined effect of all the structural variables on the overall transport properties is not possible. However, it can be emphasized that nanoclay induced reduced mobility of polymer chains and consequent decrease in free volume seem to act as additional mechanisms towards lowering the gas permeability of nanocomposites.

Conclusion

The focus of this paper was to investigate the transport mechanisms of polyurethane/clay nanocomposites beyond tortuosity effects of nanoclay. The polybutadiene polyurethane matrix was found to be a model host matrix to deduce morphology-transport relationships for its nanocomposites. Immobilization of polymer chains on the surface of nanoclay leads to a constrained amorphous region fraction which differs markedly in its molecular packing and fractional free volume. AFM topographic

imaging enabled direct visualization of the morphology of the segmented polyurethane/clay nanocomposites and the spatial extent of the constrained region. A rule of mixture analysis of fractional free volume showed that the constrained region has 58% lower free volume than the bulk amorphous region. An experimentally measurable parameter for an amorphous polymer of the average molecular interchain spacing $<R>$ in angstroms could be deduced from WAXD, which could be treated as chain segment immobility parameter. These findings together put a renewed emphasis on the role of interfacial phenomena on the transport properties in tandem with the already established tortuosity effects of nanoclay. The experimental results reveal that it is necessary to take into consideration the effect of these structural aspects to understand the gas permeability in the nanocomposite besides the tortuous diffusional path effects attributed to the clay platelet like morphology.

Nomenclature

τ	positron or positronium lifetime in PALS measurement
R	radius of free volume hole
ΔR	thickness of electron layer in which the positron in *o*-Ps annihilates
P	permeability coefficient
L	membrane thickness
N	steady-state penetrant flux
α	aspect ratio of clay particles
O	orientation parameter of the clay platelets
$I(q)$	intensity of scattered x-rays
q	scattering vector
L	interdomain distance of hard segment domains
FFV	fractional free volume
C	volume fraction of polymer chains constrained in polymer
Φ	volume fraction of clay,
H	gap between adjacent clay cuboids (face-to-face distance)
W	clay layer thickness
ζ	chain segment immobility factor
D	diameter of penetrants
$(\Phi L)1/2/2$	mean unoccupied distance between two chain segments
$<R>$	mean intersegmental distance

References

1. E.P. Giannelis, *Adv. Mat* .1996, 8 ,29-35.
2. P.C. Le Baron, Z. Wang, T.J. Pinnavaia, *J. Appl. Clay Sci.* 1999,15,11–29.
3. M. Alexandre, P. Dubois, Mater. Sci. Eng. 2000, 28, 1-63.
4. G. Choudalakis, A.D. Gotsis, *Eur. Polym. J.* 2009, 45, 967–984.
5. P.B. Messersmith, E.P. Giannelis, J. Polym. Sci. Part A: Polym. Chem. 1995, 33, 1047–1057.
6. A. Sorrentino, M. Tortora, V. Vittoria, *J. Polym. Sci. Part B: Polym. Phys.* 2006, 44, 265–274.
7. O. Gain, E. Espuche, E. Pollet, M. Alexandre, P.H. Dubois, *J. Polym. Sci. Part B: Polym. Phys.* 2005, 43, 205–214.
8. R.K. Bharadwaj, *Macromolecules* 2001, 34, 9189-9192.
9. C. Lu, Y. –W. Mai, *Phys. Rev. Lett.* 2005, 95, 088303-1–088303-4.
10. R. Toth, F. Santese, S. P. Pereira, D. R. Nieto, S. Pricl, M. Fermeglia, P. Posocco, *J. Mater. Chem.* 2012, 22, 5398-5409.
11. B. Alexandre, L. Colasse, D. Langevin, P. Médéric, T. Aubrey, C. Charpey, S. Marais, *J. Phys. Chem. B* 2010, 114, 8827-8837.
12. D. Adame, G.W. Beall, *Appl. Clay Sci.* 2009, 42, 545–552.
13. B. Xu, Q. Zheng, Y. Song, Y.Shangguan, *Polymer* 2006, 47, 2904–2910.
14. N. Jouault, J.F. Moll, D. Meng, K. Windsor, S. Ramcharan, C. Kearney, S.K. Kumar. *ACS Macro Lett.* 2013, 2, 371−374.
15. A. Eitan, F.T. Fisher, R. Andrews, J.C. Brinson, L.S. Schadler, *Comp. Sci. Technol.* 2006, 66, 1159-1170.
16. D. Sikdar, S. M. Pradhan, D. R. Katti, K. S. Katti, Mohanty, *Langmuir* 2008, 24, 5599-5607.
17. X. Zhang, L.S. Loo, *Macromolecules* 2009, 42, 5196–5207.
18. S.K. Rath , M. Patri, K. Sudarshan,P.K. Pujari, D.V. Khakhar, *AIP Conf. Proc.* 2010, 1313, 301-303.
19. S.K. Rath, M. Patri, D.V. Khakhar, *Prog. Org. Coat.* 2012,76, 264-273.
20. Y. Kojima, A. Usuki, M. Kawasumi, A. Okada, Y. Fukushima, T. Kurauchi, O.J. Kamigaito, *J. Mater. Res.* 1993, 8, 1185-1189.

21. D. Ciprari, K. Jacob, R. Tannenbaum, *Macromolecules* 2006, 39, 6565.

22. J.S. Shelley, P.T. Mather, K.L. DeVries, *Polyme*r 2001, 42, 5849-5858.

23. D. Fragiadakisa, P. Pissisa, L. Bokobza, *Polymer* 2005, 46, 6001–6008.

24. R. Ruggerone, V. Geiser, S. D. Vacche, Y. Leterrier, J. E. Månson, *Macromolecules* 2010, 43, 10490–10497.

25. A. Ammala, S.J. Pas, K. A. Lawrence, R. Stark, R. I.Webb, A.J. Hill, *J. Mater. Chem.* 2008, 18, 911–916.

26. Z.F. Wang, B. Wang, N. Qi, H.F. Zhang, L.Q. Zhang, *Polymer* 2005, 46, 719-724.

27. G. Choudalakis, A.D. Gotsis, *Curr. Opin. Coll. Interf. Sci.* 2012, 17, 132–140.

28. M.N. Muralidharan, S.A. Kumar, S. Thomas, *J. Memb. Sci.* 315 (2008) 147–154.

29. G.M. Russo, G.P.Simon, L. Incarnato, *Macromolecules* 2006, 39, 3855-3864.

30. M.A. Osman, V. Mittal, M. Morbidelli, U.W. Suter, *Macromolecules* 2003, 36 9851-9858.

31. P.K. Maji, N.K. Das, A.K. Bhowmick, *Polymer* 2010, 51, 1100-1110.

32. J.H. Chang, Y. U An, *J. Polym. Sci. Part B: Polym. Phys.* 2002, 40, 670–677.

33. J.M. Herrera-Alonso, E. Maranda, J.C. Little, S.S. Cox, *J. Memb. Sci.* 2009, 337, 208–214.

34. R. Xu, E. Manias, A.J. Snyder, J. Runt, *Macromolecules* 2001,34, 337-339.

35. C. Li, S.L. Goodman, R. M. Albrecht, S. L. Cooper, *Macromolecules* 21(1988) 2367-2375.

36. M. Serrano, W. J. MacKnight, E. L. Thomas, J. M. Ottino, *Polymer* 1987,28, 1667-1672.

37. M. Serrano, W. J. MacKnight, E. L. Thomas, J. M. Ottino; *Polymer* 1987,28, 1674-1679.

38. Y.-R. Yang, Z.-F. Wang , D.-N. Wang, B. Wang and C.-P. Hu, *Polym. Int.* 2004,53 931-936.

39. S.–L. Huang, J.-Y. Lai, *J. Memb. Sci.* 1995,105, 137-145.

40. Z.F.Wang, B.Wang, Y. Run Yang b, Chun Pu Hu, *Eur. Polym. J.* 2003, 39, 2345–2349.

41. M.B. Fernanda, M.B. Coutinho, M. C. Delpech, M.Elizabeth, F. Garcia, *Polym. Test.* 2002, 21,719–723.

42. S.K. Rath, V.K. Aswal,C. Sharma, K. Joshi, M. Patri, G. Harikrishnan, D. V. Khakhar, *Polymer* 2014, 55, 5198-5210.

43. P. Kirkegaard, M. Eldrup, *Comput. Phys. Commun*, 1974,7, 401-409.

44. S.J. Tao, *J. Chem. Phys.* 1972, 56, 5499-5510.

45. R.A. Pethrick, Prog. Polym. Sci.1997, 22, 1–47.

46. S.A. Stern, P.J. Gareis, T.F. Sinclair, P.H. Mohr, *J. Appl. Polym. Sci.* 1963,7, 2035-2051.

47. L.E Nielsen, *J.Macromol. Sci. A1* 1967, 929-942.

48. B. N. Jang, D. Wang, C. A. Wilkie, *Macromolecules* 2005**,**38, 6533-6543.

49. D. Fornes, D. R. Paul, Polymer 44(2003) 4993-5013.

50. K. Friedrich, *Adv. Polym. Sci.* 1983,52/53, 225-274..

51. J. Zheng, R. Ozisik, R.W. Siegel, *Polymer* 2005,46, 10873–10882.

52. J. Zheng, R. Ozisik, R.W. Siegel, *Polymer* 2006,47, 7786-7794.

53. V. K. Darrin, J. Pochan, *Macromolecules* 2004,37, 6480-6491.

54. G.M. Chen, Z.N. Qi, D.Y. Shen, *J. Mat. Res.* 2000,15, 351-356.

55. L.T. J. Korley, S.M. Liff, N. Kumar, G. H. McKinley, P.T. Hammond, *Macromolecules* 2006, 39, 7030-7036.

56. T.C. Merkel, B.D. Freeman, R.J. Spontak, Z. He, I. Pinnau, P. Meakin, A. J. Hill, *Science* 2002, 296, 519-522.

57. P.N Patil, S.K. Rath, S.K. Sharma, K Sudarshan, P Maheshwari, M Patri, S Praveen, P Khandelwal, P. K Pujari, *Soft Matter* 2013,9, 3589.

59. N Patil, K. Sudarshan, S.K, Sharma, S.K. Rath, M. Patri, P. K Pujari *ChemPhysChem* 2012,13, 3916-3922.

59. K. Sudarshan, S.K. Rath, M. Patri, A. Sachdeva, P.K. *Polymer* 2007,48, 6434-6438.

60. J.L. Sormana, J.C. Meredith, *Macromolecules* 37 (2004) 2186-2195.

61. J.T. Garrett, C.A. Siedlecki, J. Runt, *Macromolecules* 2001,34, 7066-7070.

62. P. Kurt, L.J. Gamble, K.J. Wynne, *Langmuir* 2008, 24, 5816-5824.

63. S.N. Magonov, V. Elings, V.; M. H. Whangbo, *Surf. Sci.* 1997, 375, L385–L391.

64. O.L. Manevitch, G.C. Rutledge, *J. Phys. Chem. B* 2004,108, 1428-1435.

65. V.V. Ginzburg, J. Bicerno, P.C. Christeson, A.K. Schrock, A.Z. Patashinski, *J. Poly. Sci. Part B: Polym. Phys.* 2007,45, 2123-2135.

66. G.W. Beall, New conceptual model for interpreting nanocomposite behaviour. In: T.J. Pinnavaia, G.W. Beall. (Eds), Polymer-clay nanocomposites. Wiley, New York, pp. 267-279.

67. M. Mulder, Basic principles of membrane technology, Kluwer, Dordrecht, 1991.

68. L.-S Teo, C.-Y. Chen, J.-F.Kuo, *J. Memb. Sci.* 1998,141, 91-99.

69. Y.J.Park, D.R. Paul, D.R, *J. Memb. Sci.* 1997,125, 23-39.

70. C. Maxwell, Treatise on Electricity and Magnetism, Oxford Univ. Press, London, 1873), vol. 1.

Legends to Figures and Tables

Figure 1: (A) WAXD profiles of the nanocomposites and nanoclay in the 2θ range 3-10° (B) SAXS profiles, $I(q)q^2$ vs. q, of PBDPU and its nanocomposites: $I(q)$ is the scattering intensity and q is the scattering vector.

Figure 2: FESEM micrographs of the air, substrate interfaces and cross section of PBDPU and its nanocomposites. The images for the neat PBDPU air and substrate interfaces are shown with a scale bar of 200-300 nms to highlight the phase separated morphology.

Figure 3: (A) Cross sectional SEM micrograph of PBDPU-5 **(**B**)** Elemental analysis of the same area in (A). **(**C**)** EDS compositional mapping of (A) highlighting aluminum and silicon elements, the constituents of montmorillonite type clay.

Figure 4: (A) WAXD profiles of PBDPU and its nanocomposites in the 2θ range 10-30° (B) variation of inersegemental spacing, <*R*> with constrained amorphous region fraction. <*R*> was evaluated from the peak position of the amorphous hallos from Figure 4A using Bragg's equation and the constrained amorphous region fraction data obtained from dynamic mechanical analysis were taken from our earlier paper (Reference 42)

Figure 5: Variation of the o-Ps intensity with volume fraction of constrained amorphous region

Figure 6: AFM images of A. PBPU and (B-D) PBDPU-1 at different magnifications, (E) The magnified image of PBDPU-1 with labeling of various phases, namely, the hard segment phase, the constrained amorphous region and the intercalated clay blocks. The interpretations are influenced by similar imaging analysis carried out by Sikdar *et al.* for a polyamide/clay nanocomposite (Reference 16).

Figure 7: Plot of *ln* permeability vs. reciprocal of fractional of fractional free volume for (A) He (B) N_2 and $CO_{2.}$.

Figure 8: Relative permeability of He, N_2 and CO_2 as a function of nanoclay volume fraction: (▲) experimental results and predicted results from model fitting according to Eq. 3 for O=0 (black line), O=1 (gray line). The values obtained from least square fitting fitting are given in Table 4.

Figure 9: Variation of normalized fractional free volume with volume fraction of constrained amorphous region.

Table 1: Variation of interdomain distance (*L*), basal spacing of nanoclay (*d*) and intersegmental distance (<R>) with clay loading (*L* and *d* from SAXS and <*R*> from WAXD measurements)

Table 2: Free volume parameters of PBDPU and its nanocomposites obtained from PALS

Table 3: Pure gas permeability coefficients and permselectivity values of PBDPU and its nanocomposites

Table 4: Aspect ratios of the intercalated clay platelets in PBDPU/clay nanocomposites evaluated from model fitting.

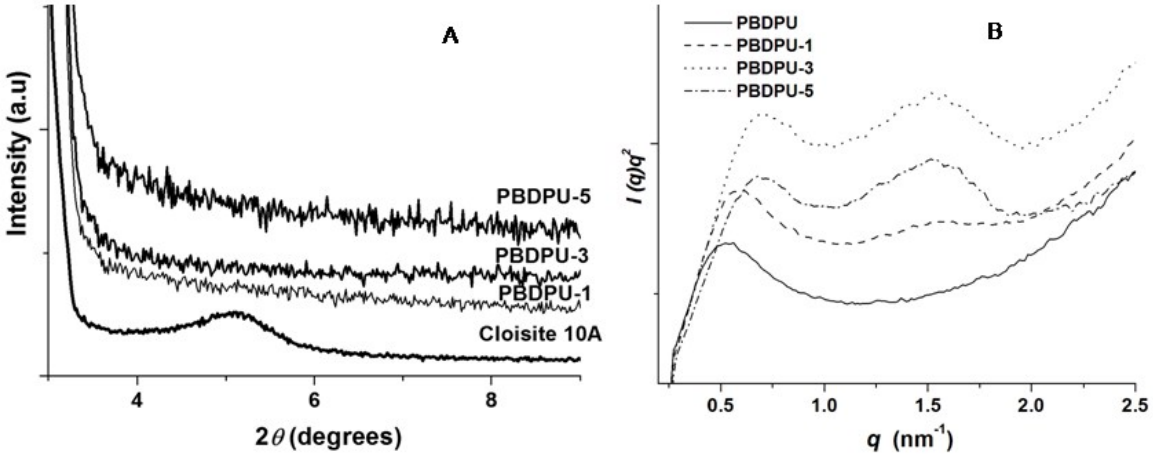

Figure 1

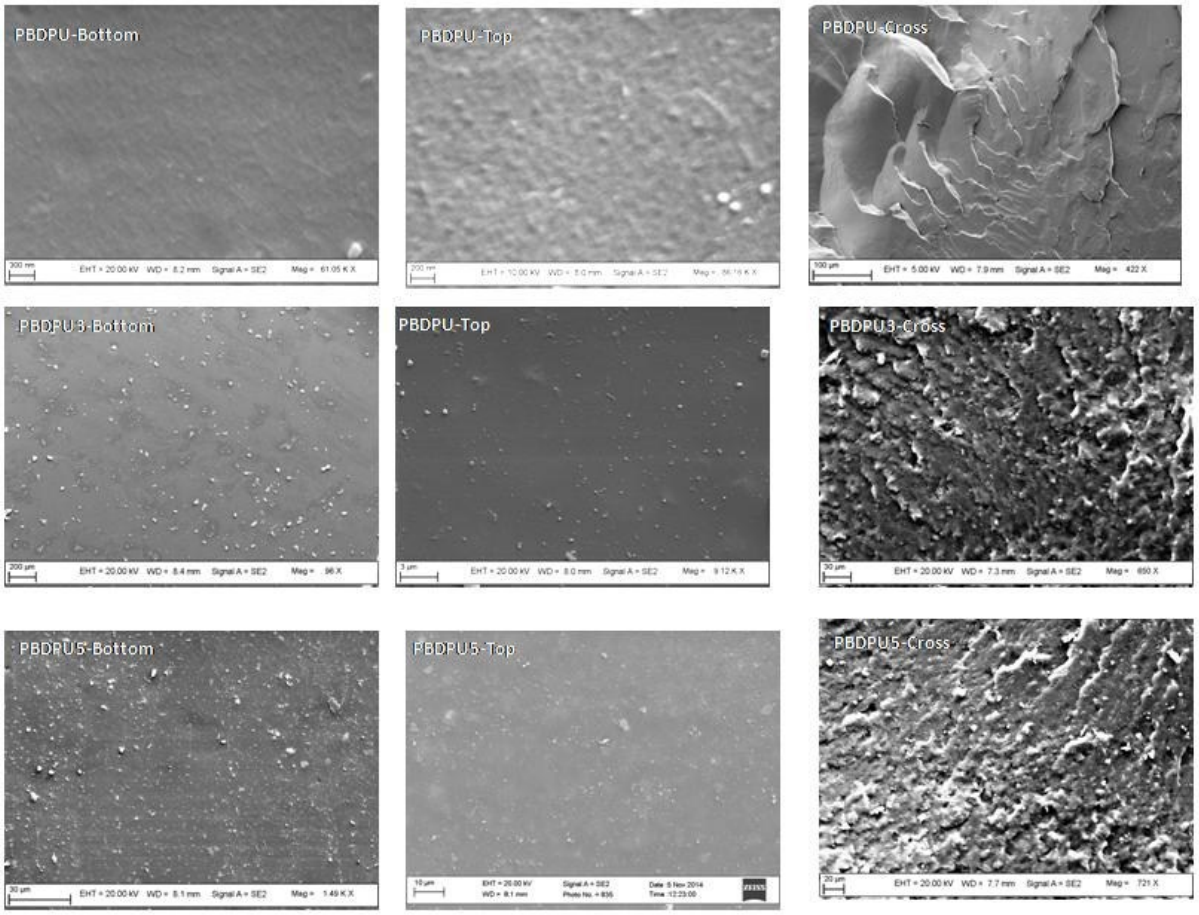

Figure 2

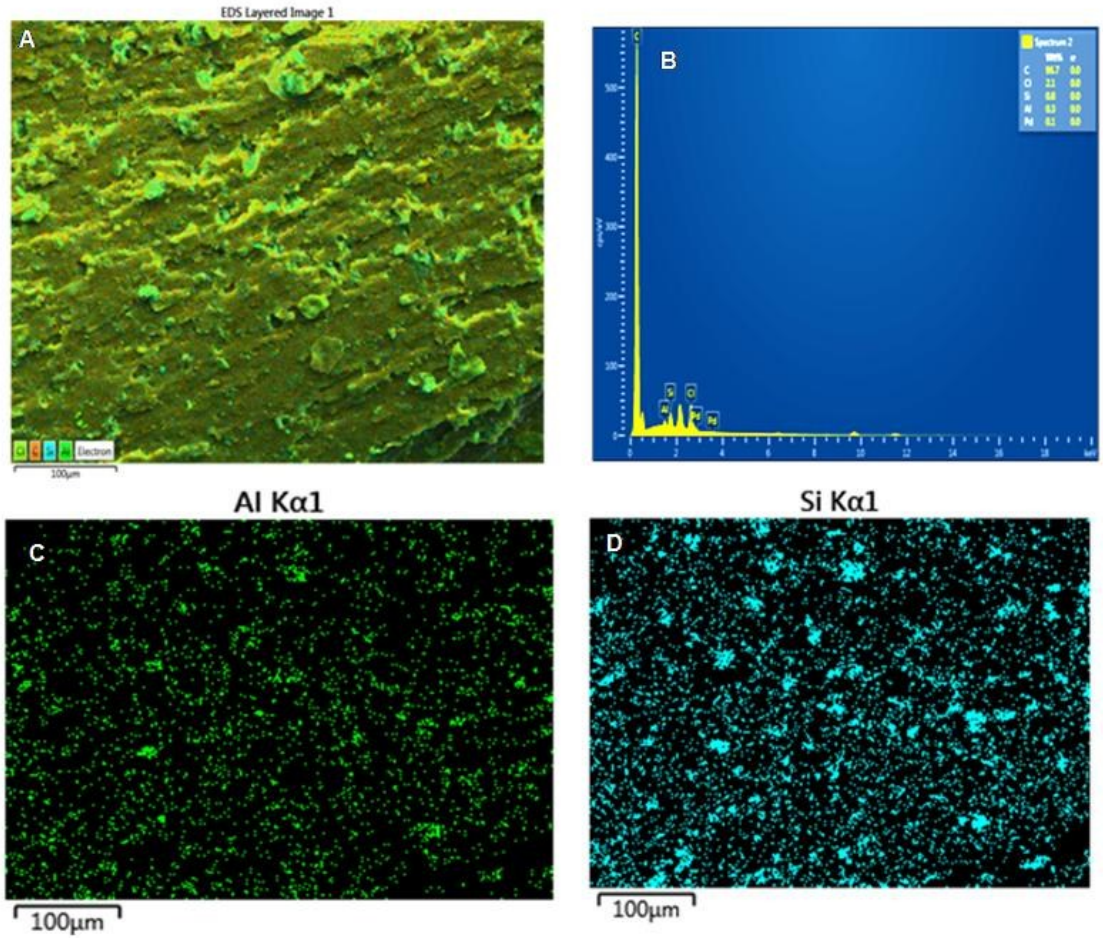

Figure 3

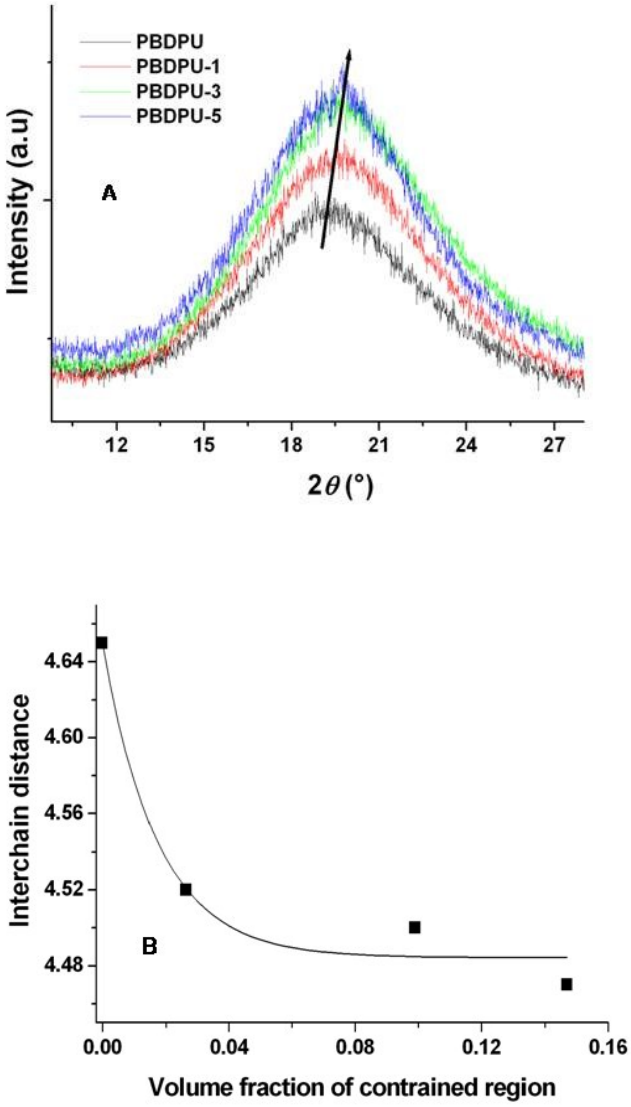

Figure 4

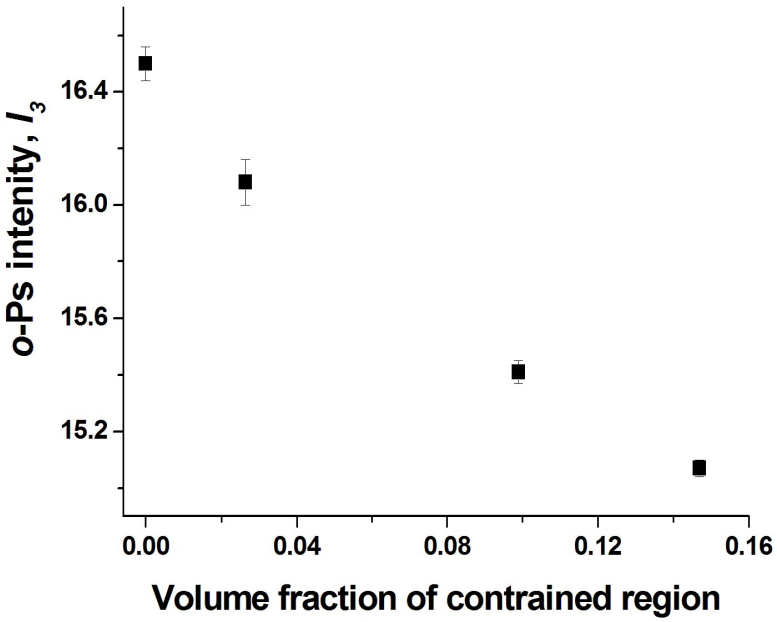

Figure 5

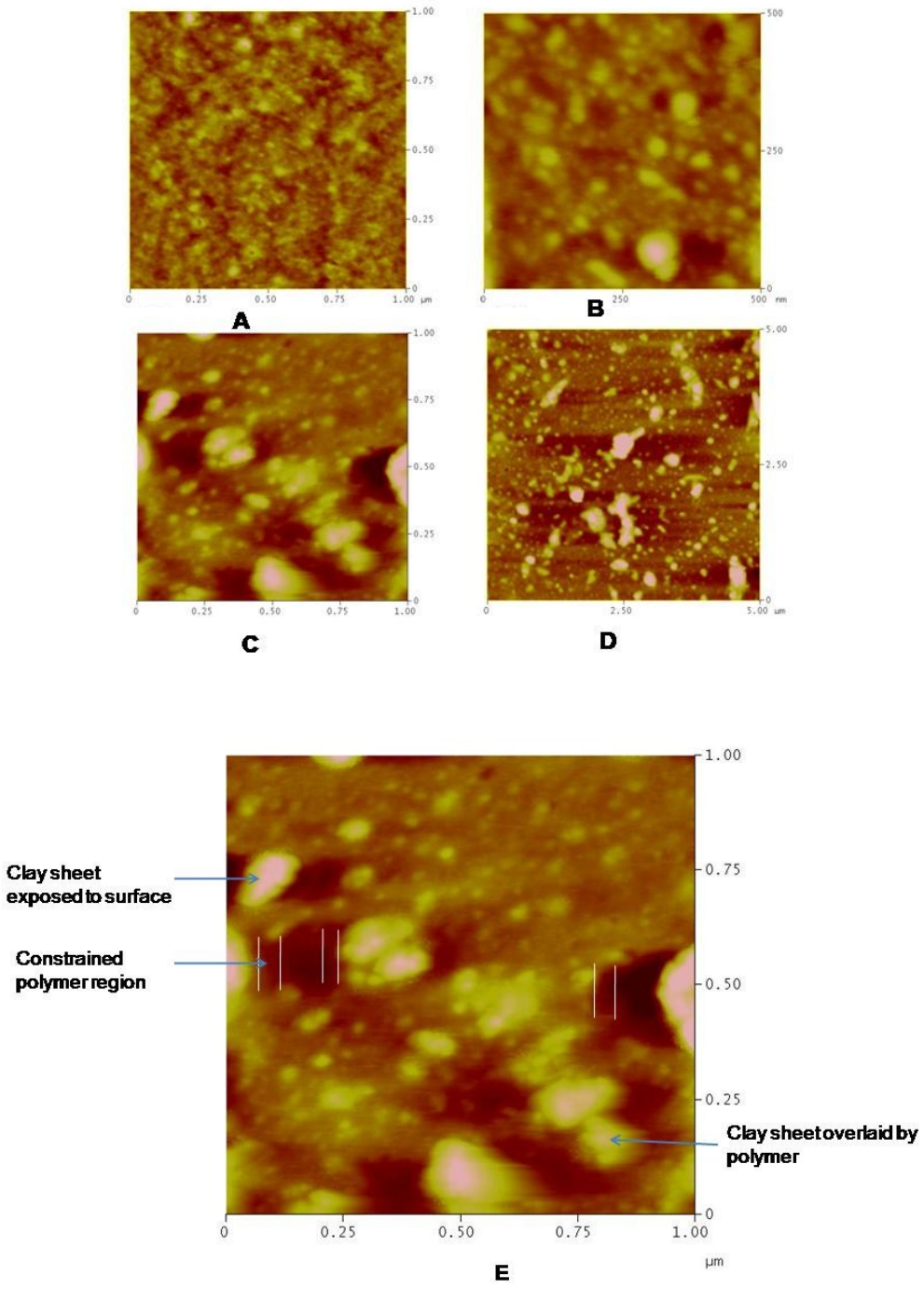

Figure 6

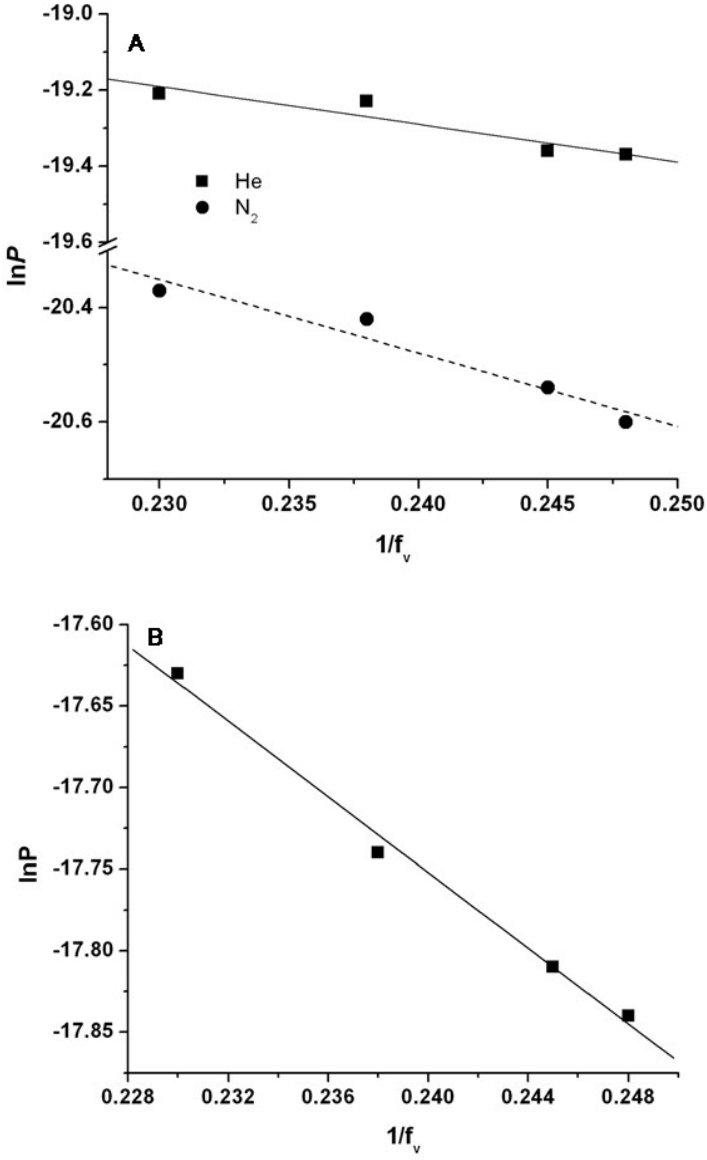

Figure 7

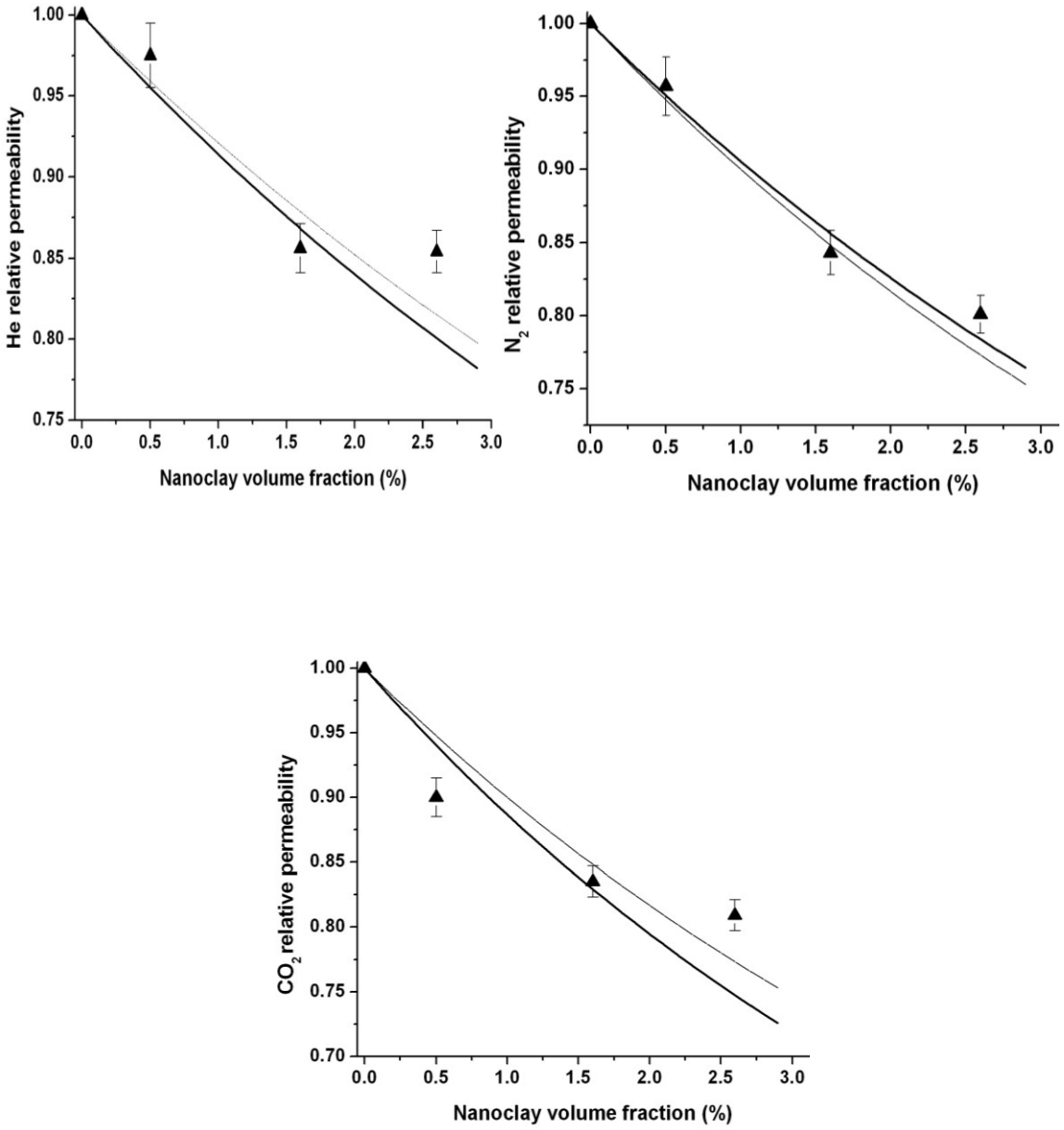

Figure 8

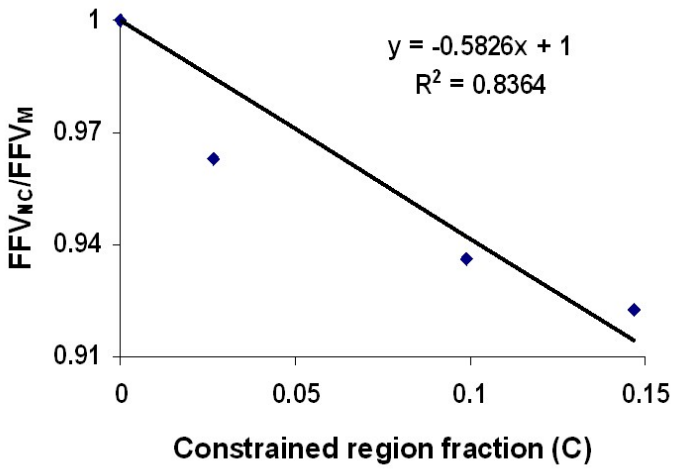

Figure 9

Table 1: Variation of interdomain distance (*L*), basal spacing of nanoclay (*d*) and intersegmental distance (<*R*>) with clay loading (*L* and *d* from SAXS and <*R*> from WAXD measurements)

Sample	(*L*) (nm)	*d*-spacing (nm)	<*R*> (Å)
PBDPU	12.1	-	4.65
PBDPU-1	11.0	4.0	4.52
PBDPU-3	9.1	4.2	4.50
PBDPU-5	9.2	4.2	4.47

Table 2: Free volume parameters of PBDPU and its nanocomposites obtained from PALS

Sample	τ_3 (ns)	I_3 (%)	Radius (Å)	f_v (%)
PBDPU	2.50 ± 0.02	16.50 ± 0.13	3.270 ± 0.01	4.36
PBDPU-1	2.48 ± 0.02	16.08 ± 0.13	3.260 ± 0.01	4.20
PBDPU-3	2.49 ± 0.02	15.41 ± 0.13	3.265 ± 0.01	4.08
PBDPU-5	2.52 ± 0.02	15.07 ± 0.14	3.30 ± 0.01	4.02

Table 3: Pure gas permeability coefficients and permselectivities of PBDPU and its nanocomposites

Sample	Permeability[a]			Permselectivity	
	P_{He}	P_{N2}	P_{CO2}	$\alpha_{CO2/N2}$	$\alpha_{He/N2}$
PBDPU	45.3	14.1	219.1	15.5	3.2
PBDPU-1	44.2	13.5	197.2	14.6	3.2
PBDPU-3	38.8	11.9	182.9	15.3	3.2
PBDPU-5	38.7	11.3	177.3	15.7	3.4

[a] Determined at 10 atm upstream pressure at 35 °C, expressed in Barrer (1 Barrer = 10^{-10} cm^3(STP).cm/cm^2.s.cm Hg)

Table 4: Aspect ratios of the intercalated clay platelets in PBDPU/clay nanocomposites evaluated from model fitting.

Permeating gas	Aspect ratio (α) *O*=1 oriented particles	Aspect ratio (α) *O*=1 random particles
He	18 ± 2	50 ± 4
N_2	20 ± 2	56 ± 3
CO_2	20 ± 2	70 ± 4